Green Chemistry

PAPER

View Article Online
View Journal

Cite this: DOI: 10.1039/d5gc06931a

Twin interfacial charge channels enable efficient photorefining of raw biomass

Fuyan Kang,[a,b,d] Chao Xu,[c] Chengfang Wang,[a] Zhanhua Huang, *[a] Hongwei Ma, *[b] Chaoji Chen *[c] and Jinguang Hu *[d]

Enhancing interfacial carrier separation and overcoming the structural recalcitrance of raw biomass are major challenges in its direct photorefining for solar fuel and platform chemical production. Here, we report a rational interfacial microenvironmental modulation strategy to construct twin charge channels in ZnS(en)/CdS photocatalysts for efficient biomass valorization. Specifically, sulfur vacancies function as electron transport pathways, while surface-coordinated ethylenediamine molecules act as hole channels, synergistically promoting interfacial charge separation and transfer. These dual channels not only facilitate carrier utilization but also activate the biomass substrate, significantly boosting photocatalytic performance. As a result, the ZnS(en)/CdS system achieves an exceptional hydrogen evolution rate of 8.89 mmol g^{-1} h^{-1} and an organic acid production rate of 5.48 mmol g^{-1} h^{-1}, both surpassing those of most previously reported photocatalysts. This work offers valuable insights into catalyst interface engineering and provides a robust strategy for advancing sustainable raw biomass photorefining.

Received 22nd December 2025,
Accepted 9th February 2026

DOI: 10.1039/d5gc06931a

rsc.li/greenchem

Green foundation

1. In this study, we report a twin charge channeling strategy for the efficient separation of photogenerated charges for raw biomass photorefining. This strategy realizes high-value, green utilization of biomass and solar energy.
2. The system enables efficient hydrogen evolution and the generation of platform chemicals (a hydrogen evolution rate of 8.89 mmol g^{-1} h^{-1} and an organic acid production rate of 5.48 mmol g^{-1} h^{-1}), advancing the research on sustainable catalysis.
3. Photorefining of raw biomass demonstrates favorable sustainability and excellent photostability, effectively reducing carbon emissions and fossil resource consumption. This work provides a research example for designing highly efficient and sustainable catalysts, demonstrating further possibilities for integrating biomass with solar energy.

1. Introduction

The urgent global challenges of climate change and energy insecurity are driving the search for sustainable alternatives to fossil fuels.[1,2] Among the potential candidates, biomass stands out due to its abundance, low cost and renewable nature.[3–5] As a result, a variety of biomass conversion pathways have been widely explored.[6] However, conventional methods such as fermentation and pyrolysis suffer from notable drawbacks, including long production times, harsh reaction conditions, and high energy consumption (Fig. S1). In contrast, biomass photorefining has recently emerged as a promising and sustainable route for converting biomass into fuels and valuable chemicals under mild conditions.[7] Photocatalysis, in particular, offers several advantages, including high selectivity, low energy input, and environmental compatibility.[8] Therefore, the development of efficient photocatalytic systems is key to advancing biomass photorefining technologies.

Among the various photocatalysts, CdS-based materials have attracted significant attention due to their ability to cleave C–C and C–O bonds in biomass through the generation of reactive radicals.[5,9–11] These materials have shown considerable promise in solar-driven biomass valorization, including hydrogen production and the synthesis of platform chemicals.[12–14] However, their practical application is hindered by rapid charge recombination and severe photocorro-

[a]Key Laboratory of Bio-based Material Science and Technology, Ministry of Education, Material Science and Engineering College, Northeast Forestry University, Harbin 150040, Heilongjiang, China. E-mail: huangzh1975@163.com
[b]Department of Chemistry and Chemical Engineering, College of Chemistry, Chemical Engineering and Resource Utilization, Northeast Forestry University, Harbin 150040, P. R. China. E-mail: mahw@nefu.edu.cn
[c]Hubei Key Laboratory of Biomass Resource Chemistry and Environmental Biotechnology, School of Resource and Environmental Science, Wuhan University, Wuhan 430079, P. R. China. E-mail: chenchaojili@whu.edu.cn
[d]Department of Chemical and Petroleum Engineering, University of Calgary, 2500 University Drive, NW, Calgary, Alberta, T2N 1N4, Canada. E-mail: jinguang.hu@ucalgary.ca

sion, both of which significantly limit their catalytic efficiency and durability.[15–17] Addressing these limitations requires the enhancement of photoinduced charge separation and stabilization mechanisms, particularly in the context of complex raw biomass feedstocks.

To overcome these challenges, various strategies have been employed to improve the photocatalytic performance of CdS, including heterojunction engineering.[18,19] Heterojunctions create internal electric fields that facilitate charge separation at the interface, thereby enhancing photocatalytic activity.[20] However, despite these improvements, charge recombination during migration remains a critical issue, especially in reactions involving raw biomass.[21–23] Recombination reduces the availability of active photogenerated species, thus limiting overall efficiency.[24,25] Therefore, enabling spatially directed charge separation and promoting rapid carrier migration and utilization are crucial for advancing photocatalytic biomass conversion.

In this work, we introduce a twin charge channel strategy by designing ZnS(en)/CdS heterostructures to overcome the challenges of charge recombination, low catalytic activity, and poor stability in traditional heterojunction systems for raw biomass photorefining (Fig. 1). This innovative dual-channel configuration enables efficient extraction and directional transport of both electrons and holes at the material interface. Specifically, sulfur vacancies and ethylenediamine (en) molecules serve as electron and hole channels, respectively, promoting charge separation and utilization. As a result, the ZnS(en)/CdS photocatalyst demonstrates significantly enhanced raw biomass photorefining performance, achieving a hydrogen evolution rate that is 2.28 times higher than those of conventional heterojunctions. Moreover, the twin charge channels improve water molecule adsorption and hydrogen desorption, further accelerating photogenerated electron utilization and hydrogen evolution. This interfacial engineering strategy not only enables efficient raw biomass photorefining but also provides a generalizable approach for designing high performance photocatalysts through interfacial microenvironment modulation.

2. Results and discussion

2.1. Sustainable raw biomass photorefining

The adsorption of water and desorption of H_2 are critical processes in raw biomass photorefining. The interactions between reacting molecules and the catalyst surface were characterized using H_2O temperature-programmed desorption (H_2O-TPD) mass spectrometry and H_2 temperature-programmed desorption (H_2-TPD). Notably, ZnS(en)/CdS-3 exhibits the largest water adsorption area and a higher desorption temperature compared to ZnS/CdS-3 (Fig. 2a). This observation reveals a stronger interaction between ZnS(en)/CdS-3 and water molecules, indicating that the introduction of twin charge channel molecules makes the catalyst more active for the adsorption of water molecules.[26] Moreover, ZnS(en)/CdS-3 exhibits a better hydrogen adsorption capacity. ZnS(en)/CdS-3 has a lower desorption temperature, which reveals more favorable hydrogen desorption (Fig. 2b).[27] These findings indicate that introducing twin charge channels alters the electronic structure and coordination environment of the material, while simultaneously enhancing the interactions at the catalytic interface among reacting molecules (Fig. 2c).

The sustainable photorefining properties of ZnS(en)/CdS were assessed using bagasse as a reaction substrate. Conditional comparison experiments demonstrated that catalysts can effectively catalyze raw biomass photorefining (Fig. S2). The catalysts demonstrated a linear variation in overall hydrogen production, indicating that the rate of hydrogen production does not significantly decrease throughout the reaction process (Fig. 2d). Moreover, the hydrogen evolution properties of the composites significantly surpassed those of

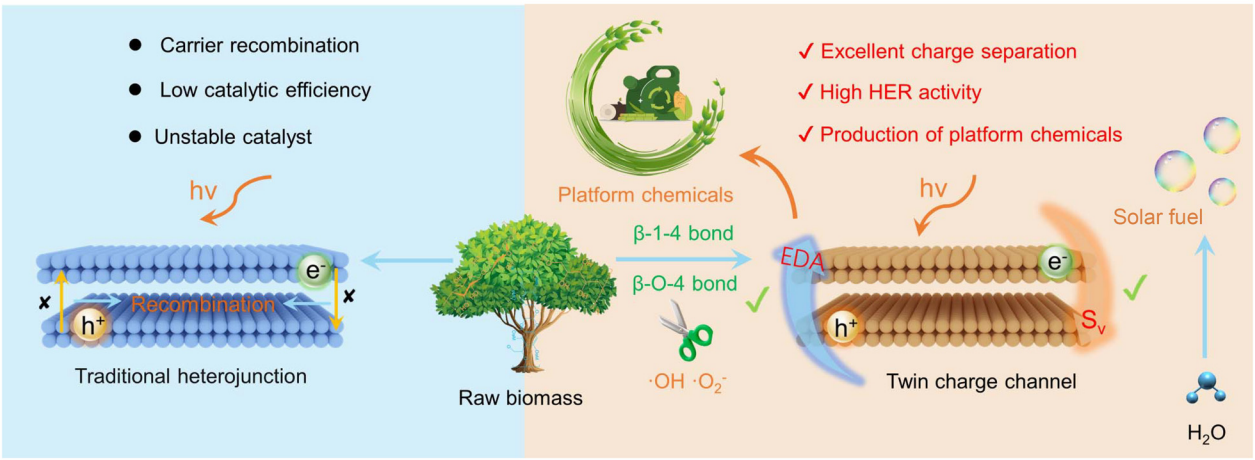

Fig. 1 Twin charge channel design concept of the ZnS(en)/CdS photocatalyst for raw biomass photorefining. Conventional heterojunctions suffer from a high carrier recombination rate, low catalytic efficiency, and poor catalytic stability. The twin charge channel enables spatially oriented separation of carriers. Solar-driven raw biomass conversion generates platform chemicals with efficient water reduction for hydrogen precipitation.

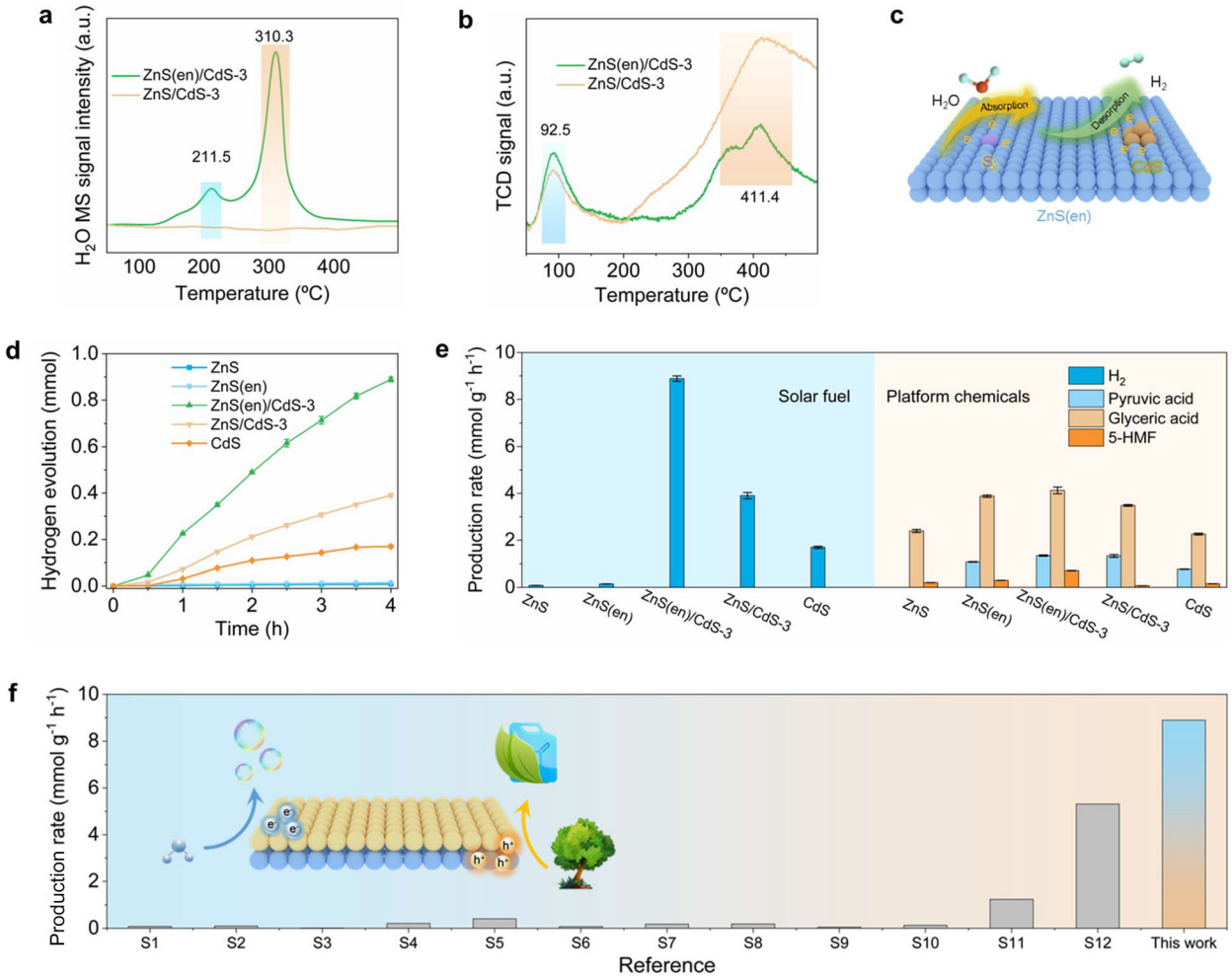

Fig. 2 Raw biomass photorefining performance of the catalyst. (a) H_2O-TPD spectra of ZnS(en)/CdS-3. (b) H_2-TPD spectra of ZnS(en)/CdS-3. (c) Adsorption of H_2O and desorption of H_2 models at the material interface. (d) Hydrogen evolution performance of the catalysts. (e) Sustainable raw biomass photorefining performance. (f) Comparison of existing working hydrogen evolution properties for raw biomass. Photorefining reaction conditions: 100 mg of bagasse, 25 mg of catalyst, DMSO : water = 25 mL : 25 mL, 5 g of NaOH, reaction time: 4 h and a 300 W xenon lamp as the light source.

individual materials such as ZnS, ZnS(en), and CdS. ZnS(en)/CdS-3 exhibits an unprecedented hydrogen production rate of 8.89 mmol g^{-1} h^{-1}. In comparison, the hydrogen evolution rate of ZnS/CdS-3 was approximately half, with a value of 3.90 mmol g^{-1} h^{-1}, relative to that of ZnS(en)/CdS-3. This phenomenon also suggested that the introduction of twin charge channels significantly enhanced hydrogen production performance in raw biomass photorefining. Further analysis of the liquid phase products revealed three main components: pyruvic acid, glyceric acid, and 5-HMF. ZnS(en)/CdS-3 demonstrates optimal bagasse conversion performance, with production rates of 1.35 mmol g^{-1} h^{-1} for pyruvic acid, 4.13 mmol g^{-1} h^{-1} for glyceric acid, and 0.70 mmol g^{-1} h^{-1} for 5-HMF. The generation of C3 products, such as pyruvic acid and glyceric acid, indicates that the catalyst effectively breaks C–C bonds in bagasse under light conditions (Fig. 2e). Additionally, the production of 5-HMF suggests that the overall reaction process involves the isomerization and dehydration of glucose. ZnS(en)/CdS exhibits better photorefining performance than other reported biomass photorefining systems (Fig. 2f, Fig. S47, and Tables S6, S7). Thus, ZnS(en)/CdS exhibits unparalleled raw biomass photorefining performance, which offers a possibility for sustainable production.

Cycling experiments were conducted to assess the photostability of the catalysts. After four cycles, the composites maintained favorable photostability (Fig. S3). Additionally, ZnS(en)/CdS-3 exhibits a low ion leaching value (0.03 mg L^{-1}, Fig. S4). This observation reveals that the photocorrosion of metal sulfides is effectively inhibited, leading to enhanced photostability. However, the yield of the liquid phase product decreased to some extent, which could be attributed to the adsorption of the product on the surface of the catalyst (Fig. S5). This finding was demonstrated by extending the cycling time to 6 hours (Fig. S6–7). Concurrently, changes in

the main component content of lignocellulose were investigated during photorefining to elucidate the reasons for the decrease in recycling performance. The amount of raw biomass significantly declined after the second cycle (Fig. S8, S9 and Table S1). Hydrogen evolution performance significantly improved upon the addition of raw biomass during the second cycle. This demonstrates that the amount of substrate further limits hydrogen evolution performance. The inherent recalcitrance of cellulose further limits photorefining performance. Qualitative and quantitative analyses of the reaction products were performed by liquid chromatography (Fig. S10 and S11). The instrument has good sensitivity (Fig. S12 and S13). The standard curves show good correlation (Fig. S14 and S15). To investigate the role of free radicals in the reaction process, ethylenediaminetetraacetic acid (EDTA), benzoquinone (BQ), terephthalic acid (TPA), and L-histidine (L-trp) were employed as scavengers for photoinduced holes (h^+), superoxide radicals ($^{\bullet}O_2^-$), hydroxyl radicals ($^{\bullet}OH$) and singlet oxygen ($^1O_2$), respectively. These scavengers exhibited varying degrees of inhibition (Fig. S16). $^{\bullet}O_2^-$ displayed the greatest inhibition of hydrogen production reactions. Meanwhile, among the platform chemical products, $^{\bullet}OH$ showed the strongest inhibitory effect (Fig. S17). The generation of $^{\bullet}O_2^-$ is related to the utilization of photogenerated electrons, thus influencing the hydrogen production reaction. Additionally, $^{\bullet}OH$ significantly influences substrate depolymerization during macromolecular biomass conversion.[24,25] These findings revealed that $^{\bullet}O_2^-$ and $^{\bullet}OH$ play key roles in hydrogen evolution reactions (HERs) and platform chemical processes, respectively.

Experiments were conducted to investigate the effects of catalysts and reaction systems on raw biomass photorefining. Among the catalysts tested, ZnS(en)/CdS-3 showed the best raw biomass photorefining performance (Fig. S18a). The ratio of catalysts does not affect the type of platform chemicals produced (Fig. S18b). The optimal dosage was also selected, with 100 mg showing the best performance (Fig. S19). Excessive biomass loading impacts the photorefining reaction in two primary ways. Firstly, it exacerbates the occurrence of side reactions and decreases the yield of the main reaction. Secondly, excessive biomass interferes with light irradiation, subsequently affecting the catalysts' ability to absorb light. Alkaline conditions play a key role in this photorefining process. Alkali affects both the HER and the yields of platform chemicals (Fig. S20). Basic conditions can effectively change the surface potential of metal sulfides, promote hole utilization and generate $^{\bullet}OH$.[28–30] At the same time, alkaline conditions promote the occurrence of dehydration and depolymerization of cellulose, along with glucose isomerization. The solvent ratio has a significant effect on photorefining performance (Fig. S21). In previous studies, we found that the main source of protons for hydrogen production is water.[31] Thus, water acts as a proton donor and accelerates photogenerated electron extraction. In the photorefining reaction, dimethyl sulfoxide (DMSO) serves multiple functions. Initially, DMSO effectively enhances the solubilization of cellulose and inhibits side reactions by facilitating product transfer. Subsequently, DMSO participates in dehydration reactions and promotes the generation of 5-HMF.[32] Experiments were performed to investigate the effect of catalyst components on the conversion of the main components of lignocellulose (Fig. S22). The catalyst effectively catalyzes the conversion of the three components. Notably, the catalyst displayed the best photorefining performance when xylan was used as the reaction substrate, compared with cellulose and lignosulfonate. This phenomenon can be attributed to the better solubility and relatively stable structure of xylan. These findings reveal that the effective photorefining of cellulose and lignin is one of the reasons limiting the total conversion performance of lignocellulose. It was also demonstrated that ZnS(en)/CdS can effectively transform the main components of lignocellulose.

2.2. Structural analysis of the twin charge channel

X-ray diffraction (XRD) spectra demonstrate the typical crystal structure of the composite material ZnS(en)/CdS (Fig. 3a and Fig. S23a). Additionally, the spectrum displays diffraction peaks from ethylenediamine (EDA) due to its coordination with zinc ions.[9,33,34] Raman spectroscopy was employed to further analyze the crystal structure of the material (Fig. S23b). The diffraction peaks at 303 cm^{-1} and 604 cm^{-1} correspond to the 1LO (longitudinal optical) and 2LO modes of CdS, respectively. The diffraction peaks at 219 and 285 cm^{-1} are assigned to the LO and transverse optical modes of ZnS.[31] Moreover, Fourier transform infrared (FT-IR) spectra of ZnS(en)/CdS reveal the presence of characteristic chemical bonds (N–H, C–H, and C–N) and functional groups (CH_2 and NH_2) associated with ethylenediamine (Fig. 3b and Fig. S24). Notably, Zn–N bonds are detected, resulting from the coordination between zinc ions and nitrogen atoms in the ethylenediamine (EDA) molecule.[35,36] These Zn–N bonds typically induce material defects, which are characterized using electron paramagnetic resonance (EPR). The EPR spectrum of ZnS(en)/CdS exhibits a typical sulfur vacancy (S_V) signal at g = 2.003 (Fig. 3c). Compared to ZnS(en), the peak intensity of ZnS(en)/CdS is reduced, indicating a higher concentration of unpaired electrons in ZnS(en) and, consequently, a greater abundance of S_Vs. The decrease in S_V concentration in the composites may be attributed to the formation of Cd–S bonds in the material, which partially fill these vacancies.[37] These results clearly demonstrate that the coordination of ethylenediamine with zinc ions leads to the formation of Zn–N bonds and, consequently, S_Vs (Fig. 3a–c).

Field emission scanning electron microscopy (F-SEM) analysis demonstrated that ZnS(en) and CdS exhibit rectangular-like nanosheet and irregular nanosheet morphologies, respectively (Fig. S25a–f, SI). ZnS(en)/CdS-3 displays the morphology of ultrathin nanosheets supported on rectangular nanosheets (Fig. S26a–c, SI). Transmission electron microscopy (TEM) analyses further confirmed the composite morphology (Fig. 3d). High-resolution transmission electron microscopy (HRTEM) provided insights into the crystal structures of the composites. Specifically, a lattice spacing of 0.31 nm corresponds to the (111) crystal plane of ZnS(en) (Fig. 3e). Meanwhile, the (101)

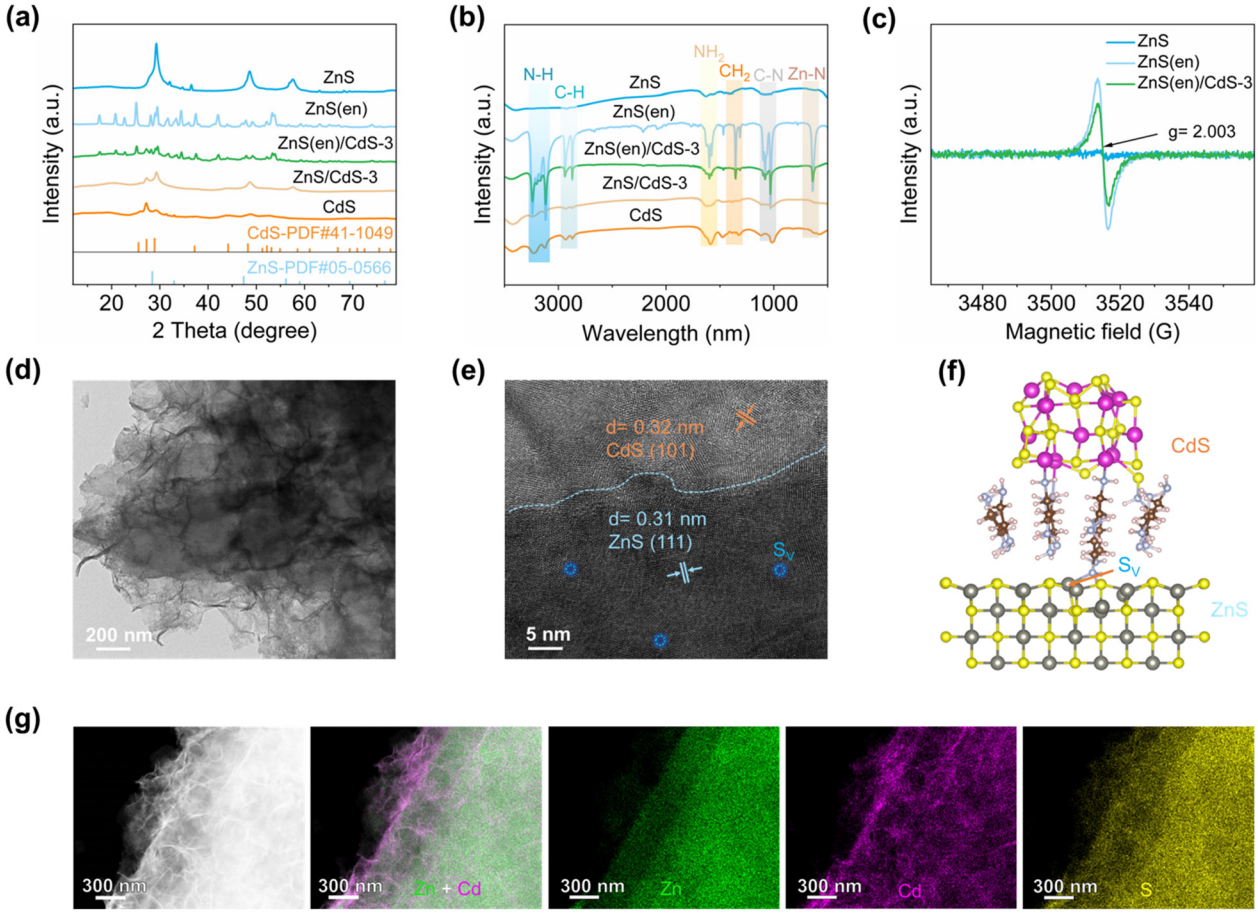

Fig. 3 Characterization of the material structure. (a) XRD pattern of ZnS(en)/CdS. (b) FT-IR spectra of ZnS(en)/CdS. (c) EPR spectra of ZnS(en)/CdS. (d) TEM and (e) HRTEM images of ZnS(en)/CdS-3. (f) Model of the crystal structure at the material interface (ash black: Zn atom; pink: Cd atom; yellow: S atom; brown: C atom; gray: N atom; and light pink: H atom). (g) EDS elemental mapping of ZnS(en)/CdS-3.

crystal plane of CdS was identified, corresponding to a lattice spacing of 0.32 nm.[38,39] The presence of lattice distortions in the ZnS(en) crystals along with the formation of S_V defects is worth noting. The amino group of the ethylenediamine molecule coordinates with the zinc ion, leading to the formation of S_Vs. Additionally, the anchoring of ethylenediamine molecules at the interface enhances the strong binding of ZnS(en) to CdS (Fig. 3f). Energy-dispersive spectroscopy (EDS) results confirmed that ultrathin nanosheets of CdS were loaded onto the ZnS(en) interface (Fig. 2g). The relevant elements were uniformly distributed in the material (Fig. S28 and S25–27).

X-ray photoelectron spectroscopy (XPS) was performed to analyze the chemical states of Zn, Cd, S, C and N elements (Fig. S29a). Zn and Cd elements exhibit valence states of +2 in the material (Fig. S29b and c).[40,41] In the S 2p spectrum, two main peaks at 162.4 and 161.1 eV are identified as S $2p_{1/2}$ and S $2p_{3/2}$ (Fig. S29d), respectively. These peaks are related to the formation of metal–sulfur bonds (Zn–S and Cd–S). Additionally, satellite peaks at 161.6 and 160.6 eV are attributed to S^{2-} and S_2^{2-}, respectively. The presence of satellite peaks (S^{2-} and S_2^{2-}) with low coordination numbers is caused by defective S_Vs.[42,43] The peaks at 284.9, 286.0 and 287.8 eV are attributed to C–C, C–N, and O=C–N bonds, respectively (Fig. S29e).[44] In the N 1s spectrum, the peak at 399.6 eV corresponds to N 1s (Fig. S29f).[45] This indicates that the increased binding energies of Zn, C, and N elements are associated with a reduction in electron density at the ZnS and EDA material interface, resulting in electron loss.[46] Conversely, the binding energy of elemental Cd decreases, implying an increase in the electron density and the acquisition of electrons at the interface. These results further imply that the electrons from ZnS(en) migrate to CdS at the material interface. The XPS data confirm the presence of S_Vs, consistent with the insights derived from previous data (Fig. 3a–d).

The N_2 adsorption–desorption isotherms display typical Type IV isotherms and H3 hysteresis loops, indicating a mesoporous structure within the material (Fig. S30a). This observation is further confirmed by the pore size distribution map (Fig. S30b). Additionally, the composite material has a large specific surface area and pore volume, which are advantageous for the photorefining reaction (Table S2). ZnS(en)/CdS exhibits absorption properties in the UV and visible range, demonstrating a broad spectrum of UV-visible absorption capabilities (Fig. S31). This suggests the effective utilization of light for raw biomass photorefining reactions (Table S3).

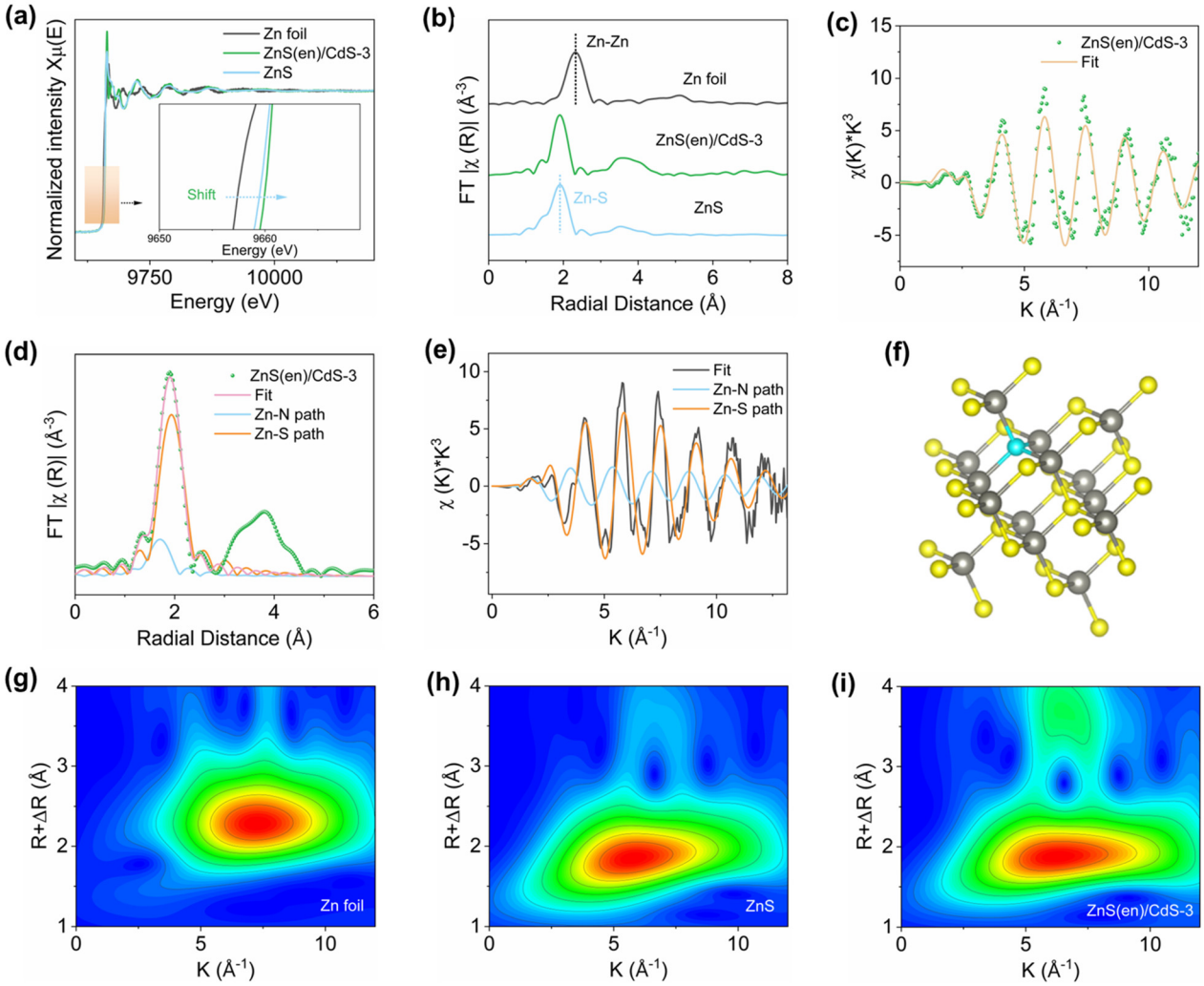

Fig. 4 Atomic microenvironmental analysis of ZnS(en)/CdS-3. (a) Zn K-edge XANES spectra. (b) Fourier transform of K-edge k^3-weighted EXAFS spectra in *R* space. (c) EXAFS fitting curve of ZnS(en)/CdS-3 in k^3 weighted *k*-space. (d) *R* space of ZnS(en)/CdS-3. (e) k^3 weighted *k*-space of the fitted data. (f) Zn atomic coordination environment in ZnS(en) (cyan: N atom, yellow: S atom, and gray: Zn atom). (g)–(i) Wavelet transform of k^3-weighted EXAFS spectra.

2.3. Interfacial atomic microenvironment explanation

The local atomic environment and electronic structure of Zn element in ZnS(en)/CdS-3 were studied using X-ray absorption fine structure spectroscopy (XAFS). The Zn K-edge X-ray absorption near-edge structure (XANES) spectrogram reveals that the Zn absorption edge of ZnS(en)/CdS-3 is located between that of ZnS and ZnO, indicating that elemental Zn is present in the +2 valence state in ZnS(en)/CdS-3 (Fig. 4a and Fig. S32a). Meanwhile, compared with ZnS, elemental Zn exhibits higher energy levels in ZnS(en)/CdS-3, indicating that the preparation of the composite changes the surrounding electronic structure.[47] This phenomenon arises from the formation of Zn–N bonds, which reduce the electron density around Zn. In the Fourier transform (FT) extended X-ray absorption fine structure (EXAFS) spectrum, the peak of ZnS(en)/CdS-3 near 1.9 Å is attributed to Zn–S bonds. In contrast to Zn foil and ZnO, Zn–Zn and Zn–O bonds are not found in ZnS(en)/CdS-3 (Fig. 4b and Fig. S32b). Additionally, ZnS displays two dominant ligand shell layers, with the second shell layer at around 3.5 Å attributed to Zn–S–M (M = Zn and Cd) bonds. The coordination environment of Zn atoms was further quantified by fitting the EXAFS spectra to ZnS(en)/CdS-3. Distances of 2.2 Å and 2.4 Å from the central atom can be assigned to Zn–N and Zn–S bonds, respectively (Fig. 4c–e). Also, the nitrogen and sulfur atoms exhibit coordination numbers of 1.1 and 3.6, respectively (Fig. 4f–i, Fig. S33, 34 and Table S4).[48] Zn atoms in the material are coordinated with nitrogen atoms from ethylenediamine molecules to form Zn–N bonds. The formation of Zn–N bonds changes the electronic structure and atomic environment around Zn.

2.4. Migration mechanisms of the twin charge channel

The interfacial charge transfer behavior of the materials was investigated by XPS under light conditions. Compared with dark

conditions, the binding energies of Zn element increase, while those of Cd decrease (Fig. 5a). This phenomenon indicates that ZnS(en) electrons migrate to CdS at the interfaces.[49] Meanwhile, under light conditions, the binding energies of C and N elements increase, while the binding energy of S element decreases (Fig. 5a). This suggests that EDA and S_Vs serve as hole and electron channels, respectively, in the raw biomass photorefining reaction. These findings support the migration of ZnS electrons to CdS and highlight the pivotal role of the twin charge channel in electron separation and migration.

The carrier dynamics of photocatalysts was characterized by photoluminescence (PL) and time-resolved photoluminescence

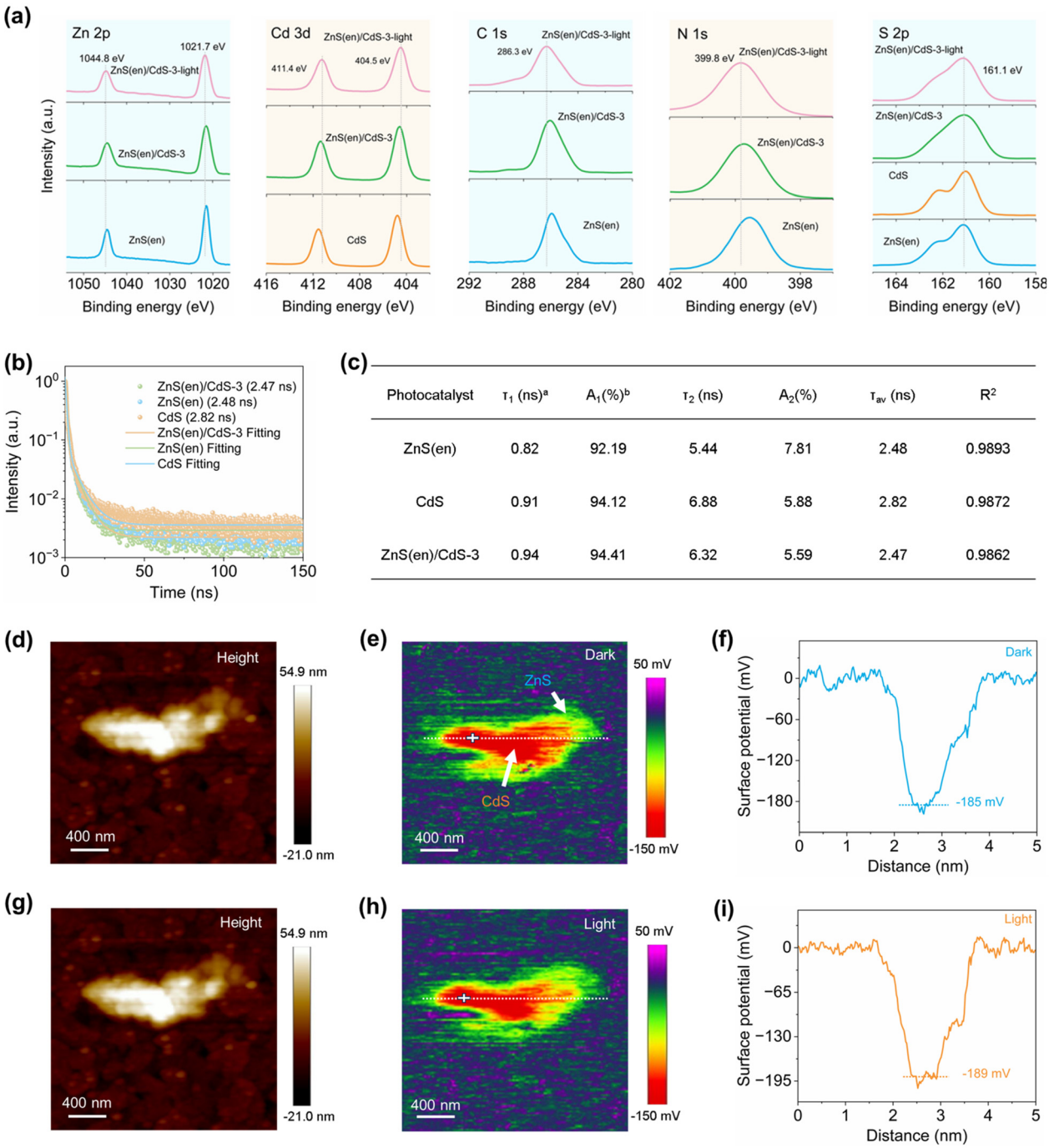

Photocatalyst	τ_1 (ns)[a]	A_1(%)[b]	τ_2 (ns)	A_2(%)	τ_{av} (ns)	R^2
ZnS(en)	0.82	92.19	5.44	7.81	2.48	0.9893
CdS	0.91	94.12	6.88	5.88	2.82	0.9872
ZnS(en)/CdS-3	0.94	94.41	6.32	5.59	2.47	0.9862

Fig. 5 Photogenerated carrier dynamics of the twin charge channel. (a) High-resolution XPS of ZnS(en)/CdS-3 in the dark or under xenon lamp irradiation. (b) Time-resolved photoluminescence (TR-PL) spectra of ZnS(en)/CdS. (c) The fitted fluorescence decay components of the as-prepared photocatalysts ([a] τ refers to the decay lifetime; [b] A represents the amplitude of decay). (d) and (g) AFM topography of ZnS(en)/CdS-3. (e) KPFM images in the dark. (f) Surface potential profiles in the dark. (h) KPFM image profiles in the light. (i) Surface potential image in the light.

(TR-PL) spectroscopy. ZnS(en)/CdS-3 demonstrated the lowest fluorescence intensity, indicating a low recombination rate of photogenerated carriers and effective separation of photoinduced charges (Fig. S35). The TR-PL spectra revealed that ZnS(en)/CdS-3 has the shortest fluorescence lifetime (2.47 ns).[50] This demonstrates that the construction of composites can effectively separate and migrate photogenerated charges (Fig. 5b and c). These findings highlight that ZnS(en)/CdS-3 has excellent photoelectric properties and is an ideal photocatalyst. Photoelectrochemical tests were performed to understand charge interface migration. ZnS(en)/CdS-3 exhibits the maximum photocurrent density (Fig. S36a), showing effective separation and migration of photoinduced charges in ZnS(en)/CdS. Meanwhile, electrochemical impedance spectroscopy (EIS) characterization revealed that ZnS (en)/CdS-3 has minimal interfacial resistance (Fig. S36b), suggesting efficient interfacial charge migration.[51] Linear sweep voltammetry (LSV) curves also further demonstrate that the composite has a small overpotential (−0.55 eV *vs.* Ag/AgCl), which reveals that the material exhibits excellent hydrogen evolution properties (Fig. S37).[52] Zeta potential tests provided insights into the charge characteristics of material surfaces (Fig. S38). The surface potential of the composite material is significantly increased compared with single materials. This reveals that the construction of the internal electric field of the material promotes the separation of charges. Mott–Schottky curves of the materials reveal flat band potentials (E_{fb}) of −1.16 and −0.61 eV (*vs.* NHE) for ZnS(en) and CdS (Fig. S39), respectively. Thus the ZnS(en) and CdS conduction band (E_{CB}) potentials are determined to be −1.26 eV and −0.71 eV (*vs.* NHE), respectively. Based on empirical equations ($E_{VB} = E_g + E_{CB}$), the valence band potentials (E_{VB}) of ZnS(en) and CdS are determined to be +3.2 and +1.86 eV (*vs.* NHE), respectively (Table S3).[53]

Achieving spatial separation and migration of interfacial charges is crucial for the photocatalytic properties of materials.[54,55] The technique of *in situ* characterization is applied to investigate interfacial charge transport. Atomic force microscopy (AFM) reveals the surface morphology of materials (Fig. 5d and g). The results showed that the surface of the samples had certain heights (−21 nm to 54.9 nm), proving that the composites are typically three-dimensional structures. Subsequently, *in situ* interfacial charge transfer under light irradiation was tested using Kelvin probe force microscopy (KPFM). The surface potential of the material was investigated in light and darkness. Analysis of CdS and ZnS (en) surfaces showed predominantly negative and positive signals (Fig. 5e and h). This reveals that electrons and holes accumulate on CdS and ZnS(en), respectively. This phenomenon is further enhanced under light conditions (Fig. 5f and i). Furthermore, the negative signal of the surface potential of CdS was also enhanced under light conditions (−185 to −189 mV), suggesting enhanced electron migration from ZnS (en) to the surface of CdS, thereby promoting the accumulation of electrons.

2.5. Mechanism of raw biomass photorefining on ZnS(en)/CdS

Density functional theory (DFT) calculations were performed to gain insight into the structure and properties of materials, particularly focusing on the band gap structure of the material. The theoretical band gap structures of ZnS, ZnS(S_V) and CdS were 2.31, 1.24 and 1.08 eV, respectively (Fig. 6a, b and Fig. S40). ZnS(S_V) was found to form a new defect energy gap due to the introduction of S_Vs. Fermi energy level calculations of ZnS (2.37 eV) and ZnS(S_V) (2.35 eV) further confirm that defect formation alters the band gap structure of the material. These new defect energy levels are anticipated to act as electron traps, promoting photogenerated charge separation and accelerating the migration of photogenerated electrons.[56] At the same time, the defect energy levels are also anticipated to promote the electron leaps in the E_{VB} of ZnS to further separate the charges. The density of states (DOS) of ZnS and CdS was analyzed. In ZnS, the valence band below the Fermi energy level mainly consists of sulfur atoms, and the conduction band below that mainly consists of Zn and S atoms (Fig. S41a). Conversely, in CdS, the valence band is mainly composed of sulfur atoms and the conduction band is mainly formed by Cd and S atoms (Fig. S42b). These data demonstrate the role of sulfur vacancies in promoting charge separation and accelerating electron transition and migration. S_Vs play the role of electron channels in the photorefining process.

Theoretical models of the material were constructed using DFT (Fig. S42), allowing for a detailed examination of the variation of electron density at the ZnS(en)/CdS interface through the computation of charge density difference (Fig. 6c). The charge density difference reveals that EDA molecules at interfaces are more prone to electron loss. This observation indicates that EDA promotes the separation of charges at the interface, accelerating the migration of holes and acting as a hole channel. Combining the experimental results and theoretical calculations, we propose the concept of the twin charge channel.

The EDA molecule forms a S_V with zinc ions *via* Zn–N coordination. The S_V plays the role of an electron channel by forming new defect energy levels within the ZnS(en) material to promote charge separation and accelerate electron transition. At the same time, EDA molecules at the material interface change the interfacial charge density, enhancing charge separation and accelerating hole migration. EDA thus acts as a hole channel in the whole process. The S_V and EDA are electron and hole channels within a material, respectively. The twin charge channel approach reduces the recombination of carrier migration processes in heterojunctions. This design concept helps to solve the problems of low charge separation efficiency and high recombination rate of heterojunctions. The free radicals in photorefining were detected by electron spin resonance (ESR). The signals for $^{\bullet}O_2^-$ and $^{\bullet}OH$ increased with an increase in light illumination time (Fig. 6d), revealing that the number of free radicals gradually increased with the duration of light illumination. This finding provides further evi-

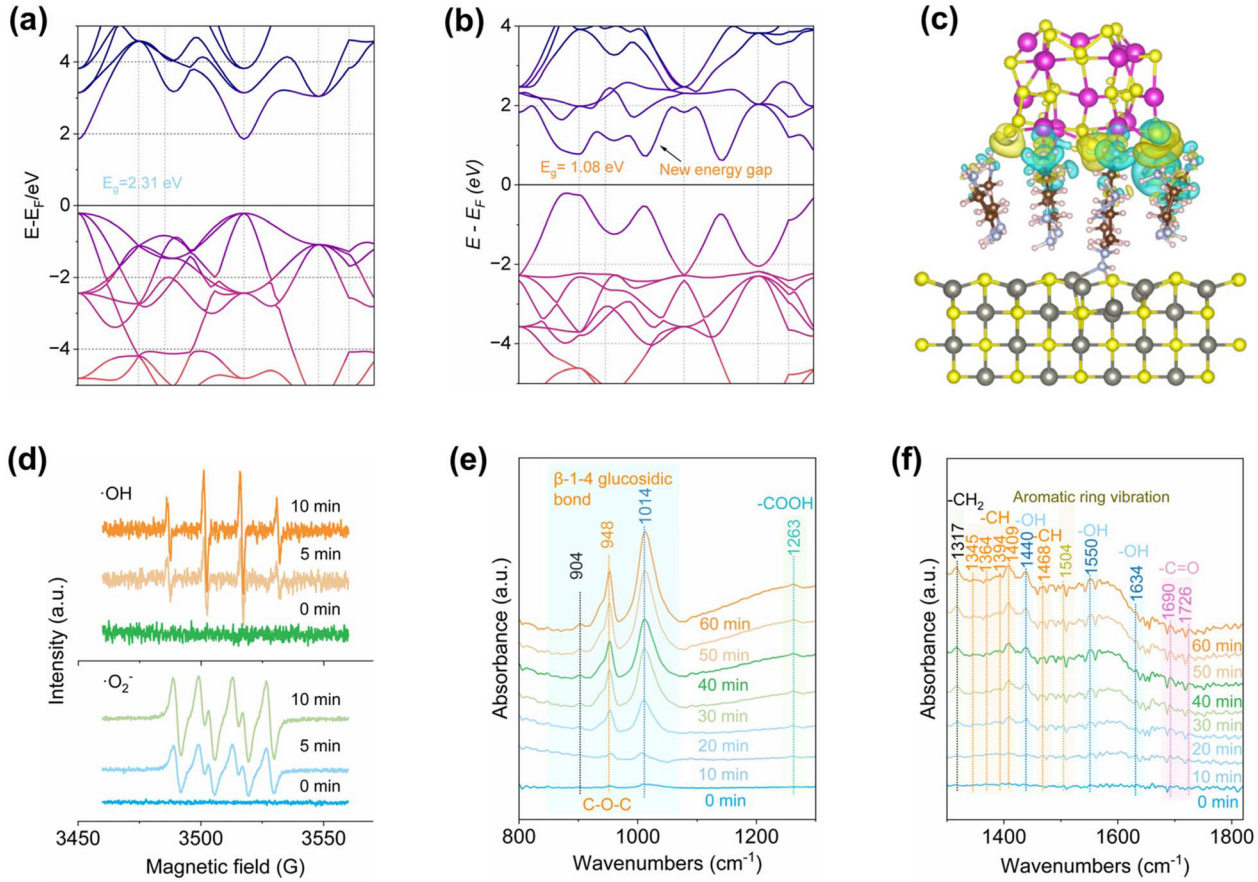

Fig. 6 Mechanisms for solar-driven refining of raw biomass. (a) and (b) Theoretically calculated bandgap structures of ZnS and ZnS(S_V). (c) The charge density difference of ZnS(en)/CdS (blue and yellow colors represent lost and gained electrons, respectively). (d) ESR spectra of $^{\bullet}O_2^-$ and $^{\bullet}OH$. (e) and (f) *In situ* FT-IR spectra at 800–1300 cm^{-1} and 1300–1800 cm^{-1}.

dence for $^{\bullet}O_2^-$ and $^{\bullet}OH$ as photorefining dominant free radicals (Fig. S16 and 17).

Raw biomass, comprising cellulose, hemicellulose and lignin, poses challenges for the exploration of photorefining mechanisms due to its complex composition. *In situ* FT-IR was used to explore the mechanisms of raw biomass photorefining. The changes in chemical bonds were observed in solar driven raw biomass conversion. In the FT-IR spectra, the changes in chemical bonds mainly occur in three ranges: 800–1300, 1300–1800 and 3200–3600 cm^{-1} (Fig. S43). The characteristic peaks within 3200–3600 cm^{-1} are mainly attributed to hydroxyl functional groups (–OH), with the peak intensity increasing over time. This indicates that the catalyst can effectively activate the hydroxyl groups in water, which further promotes the HER and the generation of free radicals. The characteristic peaks at 904, 948, and 1014 cm^{-1} are assigned to the β-1-4 glucosidic bond (C–O–C) (Fig. 6e). The strength of the glycosidic bond gradually increases with the reaction time.[57] This suggests that ZnS(en)/CdS is effective in breaking the glycosidic bond through the generated free radicals ($^{\bullet}O_2^-$ and $^{\bullet}OH$). Depolymerization of macromolecules is the rate-controlling step in biomass photorefining.[24] The characteristic peak at 1263 cm^{-1} is assigned to –COOH derived from organic acids (pyruvic acid and glyceric acid) in the product. Additionally, $-CH_2$ (1317 cm^{-1}) and –CH (1345, 1394 and 1409 cm^{-1}) functional groups correspond to the carbon chain structures in lignocellulose (cellulose, hemicellulose and lignin).[58] An increase in the intensity of characteristic peaks reveals that ZnS(en)/CdS can effectively break the C–C bonds in raw biomass (Fig. 6f). The enhanced signal of –OH (1440, 1550, and 1634 cm^{-1}) also indicates that the catalyst activates water or biomass, with a further enhancement observed during the reaction attributed to the vibration of the aromatic ring in lignin. This demonstrates that the catalyst is effective in activating lignin and breaking β-O-4 bonds. The C═O functional group comes from the product (organic acid) or the reaction substrate (lignin and hemicellulose). ZnS(en)/CdS catalysts based on the twin charge channel design effectively break β-1-4 glucosidic bonds and β-O-4 bonds in raw biomass (Fig. 6f). The generated small molecules are further functionalized *via* free radicals. Overall, the whole process enables the effective conversion of solar energy and raw biomass into platform chemicals and solar fuels.

Based on the experimental results, characterization studies, and theoretical calculations, a comprehensive mechanism for

raw biomass photorefining can be proposed. Under light irradiation, ZnS(en)/CdS undergoes energy band transition (Fig. S44 and eqn (S1)). Defective energy levels (S_Vs) in ZnS(en) promote electron transition at the E_{VB}. At the same time, S_Vs act as electron traps, accelerating electron migration and further reducing the photogenerated charge recombination rate. In this process, S_Vs function as electronic channels. EDA molecules at the interface enhance the migration of holes at the valence band of CdS to the defect energy level, serving as hole channels in this process. The electrons in the conduction band of ZnS(en) are migrating to the conduction band of CdS (eqn (S2) and (S3)). The electrons in the conduction band of CdS participate in the proton reduction reaction to produce hydrogen (eqn (S4)). Meanwhile, electrons are also involved in the reaction that generates oxygen free radicals ($^{\bullet}O_2^-$ and $^{\bullet}OH$). The hole at the defective energy level of ZnS(en) is directly involved in raw biomass conversion or in the generation of radical reactions (eqn (S5)–(S7)). Consequently, raw biomass is converted to platform chemicals upon reaction with oxygen radicals.

The proposed conversion pathways for the main components of biomass are illustrated (Fig. 7). Macromolecular sugars (cellulose and hemicellulose) cleave β-1-4 and β-O-4 bonds upon exposure to free radicals ($^{\bullet}O_2^-$ and $^{\bullet}OH$) (eqn (S8) and (S9)). The breaking of glycosidic bonds leads to the production of monosaccharides (glucose, fructose and xylose). These monosaccharides subsequently undergo C–C bond breaking and retro-aldol reactions to form 1,3-dihydroxyacetone and glyceraldehyde.[59] Pyruvaldehyde is formed through dehydration reactions, while a cross-Cannizzaro reaction between pyruvaldehyde and glyceraldehyde produces glyceric acid.[60,61] Meanwhile, pyruvaldehyde undergoes hydrogen transfer, oxidation and dehydrogenation reactions to produce pyruvic acid. Among them, C6 sugars can generate 5-HMF using a dehydration reaction.[9] The subsequent reactions are similar to the steps in the reaction of sugars to form organic acids (Fig. S45 and 46). However, platform chemical yields are lower because of the stabilizing structure of lignin.

2.6. Sustainability assessment for raw biomass photorefining

We investigated the environmental impacts of the raw biomass photorefining process using life cycle assessment (LCA). Based on this, an economic analysis of the relevant technologies was conducted to guide the direction of catalyst improvements. Two conventional bagasse conversion technologies (pyrolysis and fermentation) were compared to highlight the sustainability and characteristics of the photorefining process. In this process, we defined the cradle-to-gate analysis boundary (Fig. S48–50). The life cycle inventory (LCI) is collected, compiled, and verified in this analysis boundary (Tables S8–10). The relevant parameters of the system have been further organized and collected (input materials, energy, output products

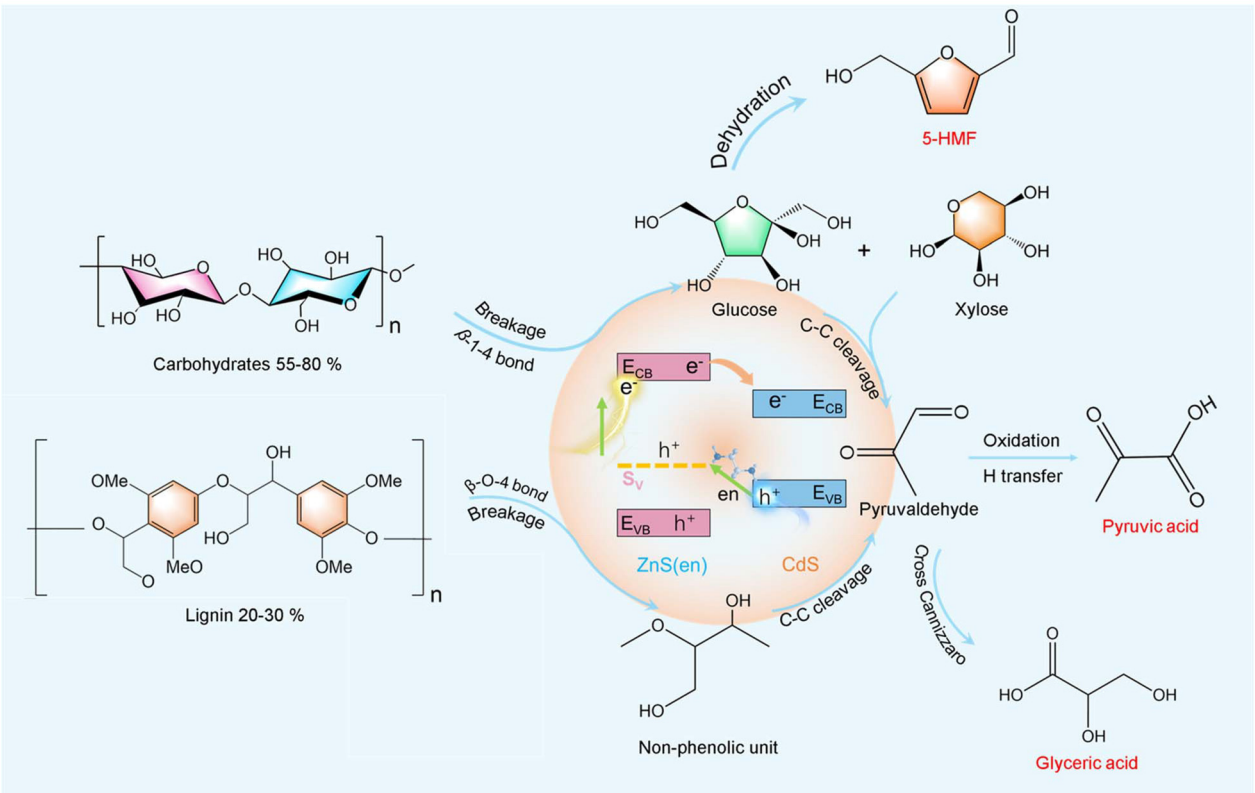

Fig. 7 Transformation pathways of the major components of lignocellulose during photogenerated charge utilization. Valorization routes of cellulose, hemicellulose, and lignin in the solar-driven ZnS(en)/CdS refining of raw biomass.

and generated waste). Based on this, we employed the ReCiPe 2016 midpoint method to analyze the environmental impacts of different technologies, specifically characterized by 20 environmental metrics (Tables S11–13). Compared to pyrolysis and fermentation processes, the photorefining process has a smaller environmental impact (Fig. 8b and Fig. S51, 52). Additionally, climate change (GWP) and fossil depletion (FDP) were further analyzed to investigate the carbon footprint and reliance on fossil fuels during the process. Photorefining technology demonstrates lower GWP and FDP scores (Fig. 8a, c and e). Throughout the process, thiourea, ethylenediamine, and dimethyl sulfoxide contributed to the majority of carbon emissions. Additionally, electricity generation accounts for a significant portion of total carbon emissions (Fig. S53). Compared to the catalyzed process, the FDP score is higher in the material preparation stage during bagasse photorefining (Fig. S54). This finding indicates that further optimization of material preparation processes is needed to reduce carbon emissions and fossil fuel consumption in future work. Compared to traditional technologies, light refining still demonstrates the lowest environmental score (Fig. 8d, f and Table S14). This demonstrates that photorefining technology has favorable sustainability, lower carbon emissions, and reduced dependence on fossil fuels.

Based on the LCA, we further conducted an economic analysis of the relevant processes. Photorefining technology has demonstrated promising economic benefits (6.03 ¥, Tables S15–17 and Fig. S55–58). Some reagents (DMSO, cadmium acetate and thiourea) constitute a major expense in the cost structure (Fig. S59). Meanwhile, platform chemicals (5-HMF, glyceric acid and pyruvic acid) are the primary products that generate profit. 5-HMF exhibits the highest value among the platform chemicals (Table S17). These results provide guidance for optimizing subsequent research work. First, material

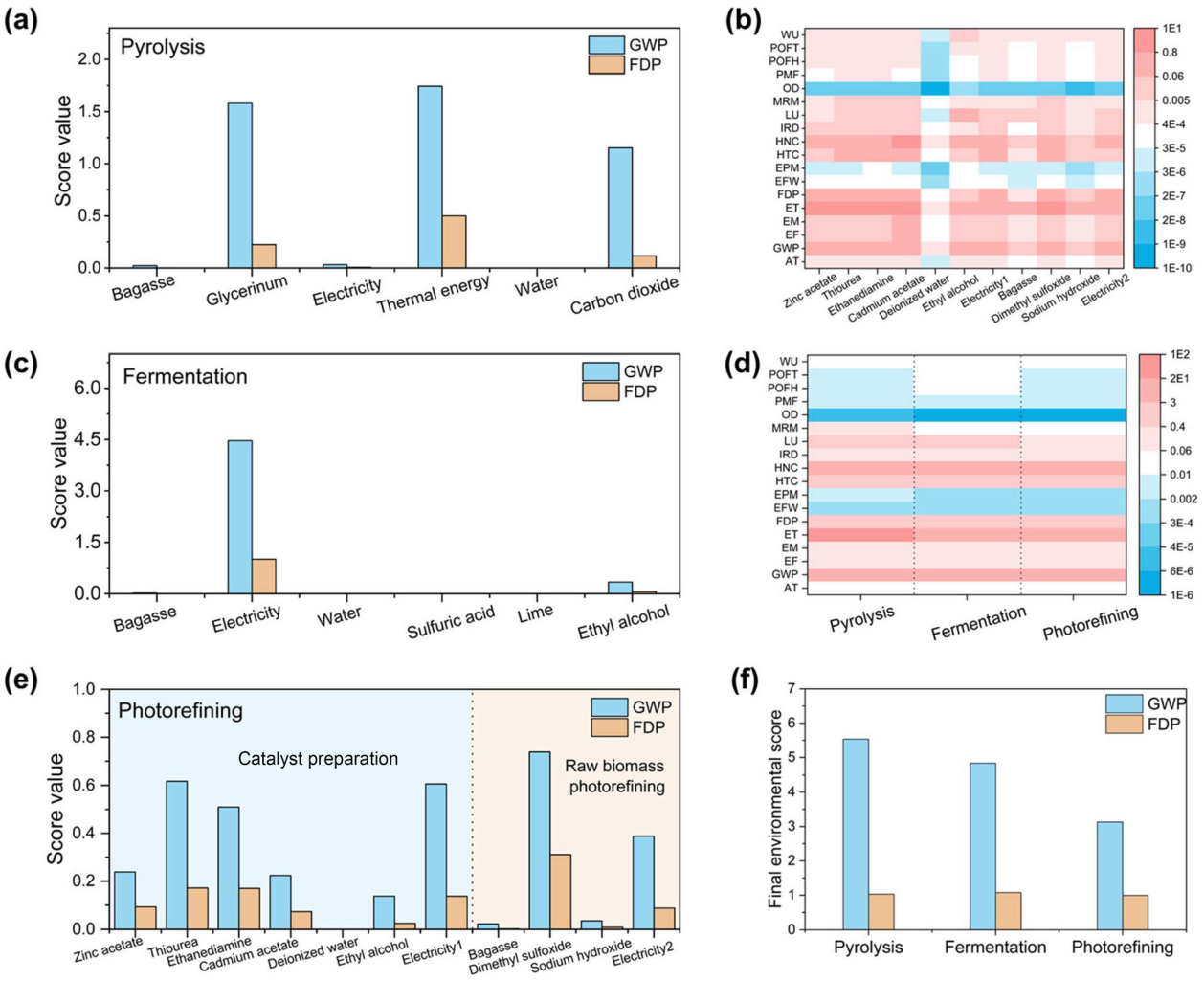

Fig. 8 Exploration of the sustainability of raw biomass photorefining. (a) GWP and FDP scores for pyrolysis related process variables of bagasse. (b) Environmental assessment of the bagasse photorefining process variables. (c) GWP and FDP scores for fermentation-related process variables of bagasse. (d) Final environmental scores for three processes (pyrolysis, fermentation and photorefining). (e) GWP and FDP scores for photorefining-related process variables of bagasse. (f) GWP and FDP for the final environmental scores of the three technologies.

preparation requires further optimization to enhance sustainability and reduce production costs in the photorefining of sugarcane bagasse. CdS-based materials and DMSO should be considered as alternatives. Second, catalytic reactions should focus on the directed functionalization of functional groups to ensure increased yields of platform chemicals. This requirement may be achieved by modifying acidic and basic sites on the catalyst surface. Furthermore, free radical processes should be controlled to prevent undesired reactions.

3. Conclusions

In this work, we developed flower-like ZnS(en)/CdS composite photocatalysts based on a twin charge channel design and applied them to raw biomass photorefining. The ZnS(en)/CdS system demonstrated exceptional performance, achieving a hydrogen evolution rate of 8.89 mmol g^{-1} h^{-1} and an organic acid production rate of 5.48 mmol g^{-1} h^{-1}, both surpassing previously reported values for similar systems. The introduction of the twin charge channel significantly reduced carrier recombination within the heterojunctions, thereby enhancing photorefining performance. Ethylenediamine (EDA) molecules anchored *via* Zn–N bonds played a critical role in constructing the twin charge channel, with sulfur vacancies (S_Vs) serving as electron channels and EDA ligands serving as hole channels. *In situ* characterization studies and theoretical calculations confirmed that this architecture facilitates spatially oriented charge separation and accelerated carrier migration, resulting in enhanced carrier utilization efficiency. Moreover, the twin channel structure enhanced water molecule adsorption and hydrogen desorption at the catalytic interface, promoting the hydrogen evolution reaction (HER). Mechanistic investigations revealed that the ZnS(en)/CdS photocatalysts effectively cleaved key β-1-4 and β-O-4 bonds in raw biomass, generating reactive radicals, crucial for conversion. Specifically, $^{\bullet}O_2^-$ and $^{\bullet}OH$ species were identified as the primary active radicals driving hydrogen evolution and biomass depolymerization, respectively. Overall, this study demonstrated that twin charge channel engineering offers a powerful and generalizable approach for designing high-efficiency photocatalysts for raw biomass photorefining, thereby advancing the sustainable production of solar fuels and value-added chemicals from renewable resources.

4. Experimental

4.1. Materials and chemicals

Cellulose, xylan, lignosulfonate, benzoquinone (BQ), L-histidine, ethylenediaminetetraacetic acid (EDTA) and terephthalic acid (TPA) were all of analytical grade and purchased from Aladdin Chemistry Co. Zinc acetate dihydrate ($Zn(CH_3COO)_2{\cdot}2H_2O$), cadmium acetate dihydrate ($Cd(CH_3COO)_2{\cdot}2H_2O$), thiourea, sodium hydroxide (NaOH), glyceric acid, and pyruvic acid were obtained. Ethylenediamine (EDA) and dimethyl sulfoxide (DMSO) were obtained from Sinopharm Chemical Reagent Co., Ltd. 5-Hydroxymethylfurfural (5-HMF) was bought from Sigma-Aldrich. Bagasse was purchased from the local market. The outer skin of bagasse was removed, the juice was pressed, and the pomace was washed six times with deionized water, dried in an oven, and subsequently pulverized to 80 mesh particle size. The contents of the main components of bagasse were analyzed using the National Renewable Energy Laboratory (NREL) method (cellulose: 36.57%, hemicellulose: 24.87% and lignin: 22.99%).

4.2. Preparation of the ZnS(en)/CdS composite

ZnS(en)/CdS was prepared by a simple solvothermal method. Initially, 0.1 g of ZnS(en) was dispersed in 30 mL of EDA solution and stirred for 30 min. ZnS(en) denotes ethylenediamine molecules coordinated on the surface and within the interlayers of ZnS. Subsequently, 1 mmol cadmium acetate dihydrate was added to the solution and stirred for 60 min. The mixed solution was transferred to a Teflon liner and reacted for 8 h at 160 °C. After completion of the reaction, the samples were collected, washed and dried. The preparation process of ZnS/CdS-3 was similar to the above process, with ZnS as a reaction material and water as a solvent. The amounts of cadmium acetate added were 0.25, 0.5, 1 and 2 mmol, and the prepared samples were denoted as ZnS(en)/CdS-1, ZnS(en)/CdS-2, ZnS(en)/CdS-3, and ZnS(en)/CdS-4, respectively.

4.3. Raw biomass photorefining

The reaction was executed in a vacuum gas circulation system under 300 w xenon lamp irradiation (Hxuv300 Visref, Beijing CEJ Tech. Co., Ltd). The reactor was maintained at a constant temperature by cooling circulating water to 6 °C. Typically, a mixture of 100 mg of bagasse, 25 mg of catalyst, and 5 g of NaOH was dispersed in 50 mL of a DMSO/water mixed solution (1 : 1, v/v). Air is evacuated from the reaction system using a vacuum pump. Subsequently, the reaction system was stirred under dark conditions for 30 min. After this, the system was irradiated and the hydrogen in the system was collected and detected by gas chromatography every 30 min (GC-7920, Beijing CEJ Tech. Co., Ltd) with a thermal conductivity detector (TCD) using N_2 as the carrier gas. The external standard method was used to quantify hydrogen testing. Gas detection is an online process. The gas circulates through the system *via* a built-in electric fan. The reaction was performed under vacuum.

The liquid product was filtered using a membrane (0.22 μm) and then detected by high performance liquid chromatography (HPLC, Agilent 1290 Infinity II) using ZORBAX Eclipse Plus C18 (2.1 mm × 50 mm × 1.8 μm) and Agilent Infinity Lab Poroshell 120 HILIC-Z (2.1 mm × 50 mm × 2.7 μm) columns. Organic acids and furfural were detected using a variable wavelength detector (VWD). Sugars were analyzed using an evaporative light scattering detector (ELSD).

4.4. Characterization

The morphologies of materials were characterized by field emission scanning electron microscopy (FE-SEM) (S-3400, Hitachi, Japan) and high-resolution transmission electron microscopy

(HRTEM) (JEM-2100, JEOL, Japan) at an accelerating voltage of 200 kV. X-ray diffraction (XRD) (D/max-2200VPC, Rigaku, Japan) was performed to determine the crystal structures of materials under Cu Kα radiation (40 kV, 30 mA) with a scanning range of 10–90° at a speed of 5° min^{-1}. Surface elemental compositions were analyzed by X-ray photoelectron spectroscopy (XPS) (PHI5700, Thermo Electron Corporation, USA) using non-monochromatic Al X-rays as the primary excitation source. N_2 adsorption–desorption isotherms and pore-size distributions were studied using a nitrogen adsorption analyzer (ASAP2020, Micromeritics, USA). UV-vis diffuse reflectance spectra (UV-vis DRS) of the samples were recorded using a double-beam ultraviolet–visible spectrophotometer (TU-1901, Beijing General Instrument Co., Ltd, China) using $BaSO_4$ as a reference in the scanning range of 200–800 nm. Fourier transform infrared (FT-IR) spectra were recorded using a Fourier-transform infrared spectrometer (iS10, Nicolet, USA) scanning from 4000 to 400 cm^{-1} at a resolution of 4 cm^{-1}. A Raman spectrometer (Thermo Fisher DXR) was used to characterize the surface chemical bonding information of the sample at an excitation wavelength of 380 nm. Photoluminescence (PL) spectra of solid powders were recorded using a Cary Eclipse fluorescence spectrophotometer (Agilent Technologies, Australia) at an excitation wavelength of 390 nm. The zeta potential test was performed using a Zetasizer Nano ZS (Malvern PANalytical Ltd, UK). Time-resolved photoluminescence (TR-PL) spectra were recorded using an FLS920 fluorescence lifetime spectrophotometer. Surface potentials are measured by Kelvin probe force microscopy (KPFM). The X-ray absorption spectroscopy (XAFS) study was performed at the BL14B2 beamline of SPring-8 (8 GeV, 100 mA), Japan, in which, the X-ray beam was monochromatized with a water-cooled Si (111) double-crystal monochromator and focused with two Zn-coated focusing mirrors with a beam size of 2.0 mm in the horizontal direction and 0.5 mm in the vertical direction around the sample position, to obtain XAFS spectra in both the near-edge and extended-edge regions.[1] Zn foil, ZnS and ZnO samples were used as references. The acquired XAFS data were processed according to standard procedures using the Artemis module of the Demeter software package. To obtain the quantitative structural parameters around central atoms, least-squares curve parameter fitting was performed using the Artemis module of the Demeter software package. Temperature-programmed desorption (TPD) measurements of H_2O and H_2 experiments were carried out using a Micromeritics AutoChem II 2920 chemisorption analyzer connected to a Hiden QIC-20 mass and TCD spectrometer, respectively. Atomic force microscopy (AFM) and Kelvin probe force microscopy were tested using an SPM-9700 surface probe system (Shimadzu, Japan). Electron spin resonance (ESR) spectra were recorded at room temperature using a Bruker A200 EPR spectrometer with a center field at 3398 G and an X-band microwave frequency of 9.45 GHz.

4.5. Photoelectrochemical experiments

Electrochemical impedance spectra (EIS) and photocurrent transient response (I–t) were recorded in a three-electrode system at an electrochemical workstation (CHI660E, Shanghai, China). Na_2SO_4 aqueous solution (0.50 M) was used as the electrolyte. A Pt plate and Ag/AgCl electrode were used as the counter and reference electrodes, respectively, while working electrodes were prepared by spreading a slurry of the as-prepared photocatalyst onto fluorine-doped tin oxide (FTO) glass.

4.6. Theoretical calculations and simulations

Density functional theory (DFT) calculations. First-principles calculations were carried out on the basis of periodic DFT using a generalized gradient approximation with the Perdew–Burke–Ernzerhof exchange correlation functional. The wave functions were constructed by the expansion of plane waves with an energy cutoff of 500 eV. A gamma-centered k-point of 3 × 3 × 3 or 3 × 3 × 1 was used for geometry optimization for the bulk ZnS ($ZnS(S_V)$) or CdS/en/$ZnS(S_V)$ slab. The consistent tolerances for geometry optimization are set as 1.0×10^{-5} eV per atom for total energy and 0.05 eV $Å^{-1}$ for force, respectively. In order to avoid the interaction between the two surfaces, a large vacuum gap of 15 Å has been selected in the periodically repeated slabs.

Methodology for life cycle assessment (LCA).. We used LCA for analysis to assess the sustainability of the raw biomass photorefining process. LCA is a systematic quantitative tool for analyzing the environmental impacts of processes, products, and services. This analysis process is conducted under the guidance of International Organization for Standardization (ISO) 14040 and 14044, comprising four stages: goal and scope definition, life cycle inventory (LCI), life cycle impact assessment (LCIA) and interpretation. We conducted the assessment using OpenLCA 2.x software and performed the calculations based on the ecoinvent 3.11 database using the ReCiPe 2016 methodology.

Goal, scope and functional unit. This study aims to investigate the environmental impacts of the raw biomass photorefining process to assess the sustainability of this process. Against this backdrop, we selected two traditional technologies (pyrolysis and fermentation) for comparison with the photorefining process. The process utilizes data from ecoinvent 3.11 for evaluation. The functional unit is defined as the processing of 1 kg of bagasse. This process selects the cradle-to-gate analysis boundary. This process aims to compare the environmental impacts of different manufacturing methods and therefore does not consider upstream raw material acquisition, downstream processes, the use phase, or end-of-life disposal. This boundary includes raw material inputs and energy consumption. This process does not take into account transportation and plant construction.

Life cycle inventory. LCI, as the second phase of LCA, involves collecting, compiling, and verifying environmental factors across product boundaries. The process involves energy input and output, raw material input, product output, gas emissions, wastewater discharge, and solid waste output. LCI is presented in Tables S8–S10.

Life cycle impact assessment. This process evaluates the environmental score by converting the input and output data

of the process into an environmental score by importing them into the system. A total of 20 impact categories were identified using the ReCiPe 2016 midpoint method, specifically including acidification: terrestrial (AT), climate change (GWP), ecotoxicity: freshwater (EF), ecotoxicity: marine (EM), ecotoxicity: terrestrial (ET), energy resources: non-renewable, fossil (FDP), eutrophication: freshwater (EFW), eutrophication: marine (EPW), human toxicity: carcinogenic (HTC), human toxicity: non-carcinogenic (HNC), ionising radiation (IRD), land use (LU), material resources: metals/minerals (MRM), ozone depletion (OD), particulate matter formation (PMF), photochemical oxidant formation: human health (POFH), photochemical oxidant formation: terrestrial ecosystems (POFT) and water use (WU).

Economic accounting. We conducted economic calculations for three technologies (pyrolysis, fermentation and photorefining) to illustrate the fundamental production costs and product revenues. This calculation aims to compare the benefits of technological production processes to guide future directions for technological improvements. This process does not include wastewater treatment during subsequent product sales, distribution, or production. At the same time, all three technologies utilize the sugarcane bagasse of identical quality as feedstock, and thus it is excluded from economic calculations. Since the process is executed in China, the economic accounting unit is Renminbi (¥).

Author contributions

Fuyan Kang: conceptualization, methodology, investigation, and writing – review & editing. Chao Xu: writing – review & editing and visualization. Chengfang Wang: investigation and methodology. Zhanhua Huang: conceptualization, methodology, supervision, and funding acquisition. Hongwei Ma: supervision and writing – review & editing. Chaoji Chen: supervision and writing – review & editing. Jinguang Hu: supervision and writing – review & editing.

Conflicts of interest

The authors declare no competing financial interest.

Data availability

Data will be made available on request. The data supporting this article have been included as part of the supplementary information (SI). Supplementary information is available. See DOI: https://doi.org/10.1039/d5gc06931a.

Acknowledgements

This work was financially supported by the Key Projects of the National Natural Science Foundation of China (No. 32430071), the Key Projects of the Natural Science Foundation of Heilongjiang Province (No. ZL2024C025), and the Key Research and Development Program of Heilongjiang Province (No. GZ20230031). Meanwhile, the authors would like to gratefully acknowledge the support from the Fundamental Research Funds for the Central Universities (2572024AW07).

References

1 G. Hayes, M. Laurel, D. MacKinnon, T. Zhao, H. A. Houck and C. R. Becer, *Chem. Rev.*, 2023, **123**, 2609–2734.
2 S. Bhattacharjee, S. Linley and E. Reisner, *Nat. Rev. Chem.*, 2024, **8**, 87–105.
3 Z. Wang, H. Ye, Y. Li, B. Sheng, P. Wang, P. Ou, X. Y. Li, T. Yu, Z. Huang, J. Li, Y. Yu, X. Wang, Z. Huang and B. Zhou, *Nat. Commun.*, 2025, **16**, 1002–1012.
4 C. T. Palumbo, E. T. Ouellette, J. Zhu, Y. Roman-Leshkov, S. S. Stahl and G. T. Beckham, *Nat. Rev. Chem.*, 2024, **8**, 799–816.
5 Z. Zhang, M. Wang, H. Zhou and F. Wang, *J. Am. Chem. Soc.*, 2021, **143**, 6533–6541.
6 Y. Wu, P. T. T. Nguyen, S. S. Wong, M. Feng, P. Han, B. Yao, Q. He, T. C. Sum, T. Zhang and N. Yan, *Nat. Commun.*, 2025, **16**, 846–858.
7 X. Wu, H. Zhao, M. Khan, P. Maity, T. Attas, S. Larter, Y. Yong, O. Mohammed, M. Kibria and J. Hu, *ACS Sustainable Chem. Eng.*, 2020, **41**, 15772–15781.
8 X. Wu, N. Luo, S. Xie, H. Zhang, Q. Zhang, F. Wang and Y. Wang, *Chem. Soc. Rev.*, 2020, **49**, 6198–6223.
9 F. Zhang, X. Lv, H. Wang, J. Cai, H. Wang, S. Bi, R. Wei, C. Yang, G. Zheng and Q. Han, *Adv. Mater.*, 2025, **37**, e2502220.
10 X. Wu, X. Fan, S. Xie, I. Scodeller, X. Wen, D. Vangestel, J. Cheng and B. Sels, *Nat. Commun.*, 2024, **15**, 4967–4978.
11 L. Wang, Y. Sun, F. Zhang, J. Hu, W. Hu, S. Xie, Y. Wang, J. Feng, Y. Li, G. Wang, B. Zhang, H. Wang, Q. Zhang and Y. Wang, *Adv. Mater.*, 2023, **35**, e2205782.
12 X. Wu, S. Xie, H. Zhang, Q. Zhang, B. F. Sels and Y. Wang, *Adv. Mater.*, 2021, **33**, e2007129.
13 D. W. Wakerley, M. F. Kuehnel, K. L. Orchard, K. H. Ly, T. E. Rosser and E. Reisner, *Nat. Energy*, 2017, **2**, 17021.
14 X. Wu, X. Fan, S. Xie, J. Lin, J. Cheng, Q. Zhang, L. Chen and Y. Wang, *Nat. Catal.*, 2018, **1**, 772–780.
15 J. Zhao, Y. Wang, H. Liu, R. Zhang, W. Jia, J. Zhang, Y. Sun and L. Peng, *ACS Catal.*, 2025, **15**, 3464–3474.
16 J. Liang, A. Labidi, B. Lu, A. O. T. Patrocinio, A. Sial, T. Gao, S. I. Othman, A. A. Allam and C. Wang, *Appl. Catal., B*, 2025, **367**, 125092.
17 J. Ma, A. Li, Q. Liu, L. Chen, M. Hong and R. Sun, *Appl. Catal., B*, 2025, **367**, 125101.
18 K. E. Shulenberger, M. R. Jilek, S. J. Sherman, B. T. Hohman and G. Dukovic, *Chem. Rev.*, 2023, **123**, 3852–3903.
19 J. Y. Li, C. L. Tan, M. Y. Qi, Z. R. Tang and Y. J. Xu, *Angew. Chem., Int. Ed.*, 2023, **62**, e202303054.

20 A. Li, J. Ma, M. Hong and R. Sun, *Appl. Catal., B*, 2024, **348**, 123834.
21 M. Eshete, X. Li, L. Yang, X. Wang, J. Zhang, L. Xie, L. Deng, G. Zhang and J. Jiang, *Small Sci.*, 2023, **3**, 2200041.
22 X. Tao, Y. Zhao, S. Wang, C. Li and R. Li, *Chem. Soc. Rev.*, 2023, **51**, 3561–3608.
23 C. Cheng, S. Zhang, J. Zhang, L. Guan, M. E. El-Khouly and S. Jin, *Angew. Chem., Int. Ed.*, 2024, **63**, e202411359.
24 J. Yang, H. Zhou, J. Luo and M. Wang, *ACS Catal.*, 2025, **15**, 1663–1671.
25 Q. Cheng, Y.-J. Yuan, R. Tang, Q. Liu, L. Bao, P. Wang, J. Zhong, Z. Zhao, Z. Yu and Z. Zou, *ACS Catal.*, 2022, **12**, 2118–2125.
26 J. Zhang, Y. Pan, D. Feng, L. Cui, S. Zhao, J. Hu, S. Wang and Y. Qin, *Adv. Mater.*, 2023, **35**, e2300902.
27 Q. Li, H. Wang, M. Zhang, G. Li, J. Chen and H. Jia, *Angew. Chem., Int. Ed.*, 2023, **62**, e202300129.
28 V. Nguyen, D. B. Nimbalkar, L. D. Nam, Y. Lee and H. Teng, *ACS Catal.*, 2021, **11**, 4955–4967.
29 W. Xue, X. Bai, J. Tian, X. Ma, X. Hu, J. Fan and E. Liu, *Chem. Eng. J.*, 2022, **428**, 132608.
30 W. Xue, J. Tian, X. Hu, J. Fan, T. Sun and E. Liu, *Chem. Eng. J.*, 2022, **443**, 136427.
31 F. Kang, C. Shi, Y. Zhu, M. Eqi, J. Shi, M. Teng, Z. Huang, C. Si, F. Jiang and J. Hu, *J. Energy Chem.*, 2023, **79**, 158–167.
32 J.-P. Tang, Y. Chen, Z.-Y. Wang, Y.-H. Hu, J.-H. Wang, L. Bao, Z.-Y. Zhao and Y.-J. Yuan, *ACS Catal.*, 2024, **15**, 265–274.
33 G. Li, D. An, X. Zhou and F. Wang, *ACS Catal.*, 2025, **15**, 7800–7809.
34 J. Kundu, D. D. Mal and D. Pradhan, *Inorg. Chem. Front.*, 2021, **8**, 3055–3065.
35 G. Yang, T. Chen, C. Xing, Z. Tian, Y. Hu, G. Yu and X. Li, *Appl. Surf. Sci.*, 2022, **578**, 152033.
36 H. Zhang, C. Xin, X. Wang and K. Wang, *Int. J. Hydrogen Energy*, 2016, **41**, 12019–12028.
37 T. Tian, X. Jin, N. Guo, H. Li, Y. Han and Y. Yuan, *Appl. Catal., B*, 2022, **308**, 121227.
38 Y.-W. Han, Y.-T. Chu, L. Ye, T.-J. Gong and Y. Fu, *ACS Catal.*, 2024, **14**, 17716–17726.
39 P. Li and B. Zhang, *ACS Catal.*, 2024, **14**, 18345–18353.
40 X. Chen, R. Guo, W. Pan, Y. Yuan, X. Hu, Z. Bi and J. Wang, *Appl. Catal., B*, 2022, **318**, 121839.
41 A. Moutsiou, A. Olivati, L. A. Cipriano, A. Sivo, S. M. Collins, Q. M. Ramasse, I. S. Kwon, G. Di Liberto, M. Kanso, R. Wojcieszak, G. Pacchioni, A. Petrozza and G. Vile, *ACS Catal.*, 2025, **15**, 5601–5613.
42 Z. Ye, Y. Jiang, L. Li, F. Wu and R. Chen, *Adv. Mater.*, 2022, **34**, e2109552.
43 Y. Zou, Y. Gu, B. Hui, X. Yang, H. Liu, S. Chen, R. Cai, J. Sun, X. Zhang and D. Yang, *Adv. Energy Mater.*, 2020, **10**, 1904147.
44 Q. Xue, H. Li, P. Jin, X. Zhou and F. Wang, *Angew. Chem., Int. Ed. Engl.*, 2025, e202423368.
45 L. Hao, M. Ding, S. Song, Y. You and X. Li, *Appl. Catal., B*, 2025, **374**, 125371.
46 P. Guo, X. Liu, C. You, B. Zhang, P. Zhang, Z. Xiong, H. Li, H. Zhang, R. Wang, Z. Zhang and S. Qiu, *Appl. Catal., B*, 2025, **366**, 125011.
47 Y. Wu, C. Chen, X. Yan, X. Sun, Q. Zhu, P. Li, Y. Li, S. Liu, J. Ma, Y. Huang and B. Han, *Angew. Chem., Int. Ed.*, 2021, **60**, 20803–20810.
48 Y. Sun, W. Fan, Y. Li, N. L. D. Sui, Z. Zhu, Y. Zhou and J. M. Lee, *Adv. Mater.*, 2023, e2306687.
49 J. Low, B. Dai, T. Tong, C. Jiang and J. Yu, *Adv. Mater.*, 2019, **31**, e1802981.
50 M. Zhang, Y. Zhang, L. Ye, Z. Yu, R. Liu, Y. Qiao, L. Sun, J. Cui and X. Lu, *Appl. Catal., B*, 2023, **330**, 122635.
51 D. Zu, Y. Ying, Z. Xu, G. Chen, L. Bai, S. Ahmed, Z. Lin, Y. Zhu, A. M. Saleque, S. She, M. M. Li, M. N. A. S. Ivan, H. Wu, Y. H. Tsang and H. Huang, *Appl. Catal., B*, 2023, **328**, 122494.
52 J. Ran, L. Chen, D. Wang, A. Kiakalaieh, Y. Jiao, S. Ahmed, Y. Qu, L. Jing, K. Davey and S. Z. Qiao, *Adv. Mater.*, 2023, **35**, e2210164.
53 X. Yang, F. Li, W. Liu, L. Chen, J. Qi, W. Sun, F. Pan, T. Duan and F. Sun, *Appl. Catal., B*, 2023, **324**, 122202.
54 T. Yu, J. Li, Y. Li, L. Qiu, H. Pan, L. Zhu, Z. Huang and B. Zhou, *Angew. Chem., Int. Ed.*, 2024, **63**, e202405904.
55 Y. Liu, S. Ye, H. Xie, J. Zhu, Q. Shi, N. Ta, R. Chen, Y. Gao, H. An, W. Nie, H. Jing, F. Fan and C. Li, *Adv. Mater.*, 2020, **32**, e1906513.
56 C. Du, Q. Zhang, Z. Lin, B. Yan, C. Xia and G. Yang, *Appl. Catal., B*, 2019, **248**, 193–201.
57 M. Zhong, X. Li, X. Chu, H. Gui, S. Zuo, C. Yao, Z. Li and Y. Chen, *Appl. Catal., B*, 2022, **317**, 121718.
58 F. Xu, J. Yu, T. Tesso, F. Dowell and D. Wang, *Appl. Energy*, 2013, **104**, 801–809.
59 J. Ma, D. Jin, Y. Li, D. Xiao, G. Jiao, Q. Liu, Y. Guo, L. Xiao, X. Chen, X. Li, J. Zhou and R. Sun, *Appl. Catal., B*, 2021, **283**, 119520.
60 M. Wang, H. Zhou and F. Wang, *Acc. Chem. Res.*, 2023, **56**, 1057–1069.
61 J. Wang, X. Wang, H. Zhao, J. F. Van Humbeck, B. N. Richtik, M. R. Dolgos, A. Seifitokaldani, M. G. Kibria and J. Hu, *ACS Catal.*, 2022, **12**, 14418–14428.